

RESEARCH

Open Access



hiPSC-derived cardiomyocyte to model Brugada syndrome: both asymptomatic and symptomatic mutation carriers reveal increased arrhythmogenicity

Kirsi Penttinen^{1†}, Chandra Prajapati^{1*†}, Disheet Shah¹, Dhanesh Kattippambal Rajan¹, Reeja Maria Cherian¹, Heikki Swan³ and Katriina Aalto-Setälä^{1,2}

Abstract

Brugada syndrome is an inherited cardiac arrhythmia disorder that is mainly associated with mutations of the cardiac voltage-gated sodium channel alpha subunit 5 (*SCN5A*) gene. The clinical symptoms include ventricular fibrillation and an increased risk of sudden cardiac death. Human-induced pluripotent stem cell (hiPSC) lines were derived from symptomatic and asymptomatic individuals carrying the R1913C mutation in the *SCN5A* gene. The present work aimed to observe the phenotype-specific differences in hiPSC-derived cardiomyocytes (CMs) obtained from symptomatic and asymptomatic mutation carriers. In this study, CM electrophysiological properties, beating abilities and calcium parameters were measured. Mutant CMs exhibited higher average sodium current densities than healthy CMs, but the differences were not statistically significant. Action potential durations were significantly shorter in CMs from the symptomatic individual, and a spike-and-dome morphology of action potential was exclusively observed in CMs from the symptomatic individual. More arrhythmias occurred in mutant CMs at single cell and cell aggregate levels compared with those observed in wild-type CMs. Moreover, there were no major differences in ionic currents or intracellular calcium dynamics between the CMs of asymptomatic and symptomatic individuals after the administration of adrenaline and flecainide.

In conclusion, mutant CMs were more prone to arrhythmia than healthy CMs but did not explain why only one of the mutation carriers was symptomatic.

Keywords Brugada syndrome, Human-induced pluripotent stem cell derived cardiomyocyte, Sodium, SCN5A, Arrhythmia

[†]Kirsi Penttinen and Chandra Prajapati contributed equally to this study.

*Correspondence:

Chandra Prajapati
chandra.prajapati@tuni.fi

¹Faculty of Medicine and Health Technology and BioMediTech Institute, Tampere University, Tampere 33520, Finland

²Heart Hospital, Tampere University Hospital, Tampere 33520, Finland

³Helsinki University Hospital, Helsinki 00290, Finland



Introduction

Brugada syndrome is an inherited cardiac arrhythmia disorder predisposing patients to ventricular tachycardia or fibrillation and sudden cardiac death. The diagnosis of Brugada syndrome mainly relies on specific ST elevation on surface electrocardiogram (ECG), history of ventricular tachycardia or fibrillation, family history of sudden cardiac death, and syncope occurrence [1, 2]. So far, the only effective treatment is the implantation of a cardioverter defibrillator [3], and the limited understanding of the cellular mechanisms underlying Brugada syndrome complicates the development of diagnostic and therapeutic approaches.

Brugada syndrome has been associated with mutations in 23 different genes [4]. Most mutations are in the voltage-gated sodium (Na^+) channel alpha subunit 5 (*SCN5A*) gene coding for the alpha subunit of the cardiac Na^+ channel ($\text{Na}_v1.5$) responsible for the Na^+ inward current (I_{Na}) [5]. Loss- or gain-of-function mutations in *SCN5A* result in the dysfunction of $\text{Na}_v1.5$, which leads to increased or decreased I_{Na} [6]. However, the link between a mutation and a disorder is rarely direct, and mutations in several genes can have a single clinical outcome, such as the Brugada syndrome [7]. Moreover, the clinical phenotype might differ even among carriers of the same mutation within one family, but underlying reasons for this phenotypic variability and incomplete penetrance are not always clear [7]. The human cellular phenotype of Brugada syndrome is not fully characterized because the available heterologous expression models lack many characteristics of native cardiomyocytes (CMs) and fail to fully recapitulate the disease [8]. Recently, the cellular mechanisms of Brugada syndrome have been investigated using human-induced pluripotent stem cell (hiPSC)-derived CMs (hiPSC-CMs) obtained from patients [9–17].

The hiPSC technology [18] is a valuable tool for studying genetic diseases and phenotypic variability. Here hiPSC lines were derived from two stepbrothers carrying a mutation in the *SCN5A* gene. One brother had been diagnosed with Brugada syndrome. The other one was asymptomatic, and arrhythmias could not be provoked by electrophysiological or pharmacological stimuli. We aimed to determine whether hiPSC-derived CMs (hiPSC-CMs) obtained from both stepbrothers presented different cellular phenotypes from one another and from that of healthy wild-type (WT) hiPSC-CMs.

Materials and methods

Clinical information

The pedigree of the family is presented in Fig. 1A. The symptomatic patient is a male diagnosed with Brugada syndrome and he carries the *SCN5A*-p.R1913C variant. This is likely pathogenic variant (referred later as

mutation), since it is very rare in general population, in silico models predict it to be deleterious, mutation in the same codon has been reported to pathogenic and three paralogue pathogenic mutants are known. He was 32 years old at the time of the skin biopsy. He lost consciousness for the first time at home at night while having high fever in 2005. A prominent convex ST-segment elevation was observed in V1–V4. His next syncopal spell occurred in 2013 at an ice hockey rink. Later that year, he was resuscitated from an episode of ventricular fibrillation on the street. The ECG revealed slightly concave ST-segment elevation in all chest leads (up to 2 mm in V3). A typical example of spontaneous Brugada type 1 ECG from the symptomatic individual after collapse is presented in additional file 1: Fig S1. The patient's cardiac ultrasound, magnetic resonance imaging, and coronary angiogram were always normal. An early repolarization and ST elevation in V1 and V2 (Fig. 1B) were observed in the flecainide test. Consequently, a cardioverter defibrillator was implanted. This patient also carries a R325W variant in the gene coding for the potassium inwardly rectifying channel subfamily J member 2 (*KCNJ2*-R325W). It has been associated with Andersen–Tawil syndrome, but an exercise stress test revealed no ventricular arrhythmias characteristic of Andersen–Tawil syndrome. However, the significance of the R325W variant in *KCNJ2* is not known and with current knowledge, the pathogenicity of the variant cannot be verified or ruled out and thus it is a variant of unknown significance. Our patient did not have a history of periodic paralysis, and the resting ECG revealed no prominent U waves. The stepbrother of this patient presented both *SCN5A*-p.R1913C mutation and *KCNJ2*-R325W variant of unknown significance. He was 50 years old at the time of the skin biopsy. This individual never had cardiac symptoms, and the flecainide test revealed no sign of Brugada ECG or QT interval prolongation. The father from both stepbrothers had suddenly died at the age of 53.

Generation and characterization of hiPSC lines

The hiPSC study was approved by the ethical committee of the Pirkanmaa Hospital District (R08070), and written informed consent was obtained from the participants. Skin fibroblasts were used to generate hiPSC lines. All the experiments were performed in accordance with relevant guidelines and regulations. The healthy control hiPSC line UTA.04511.WT was generated using Sendai vectors, and the healthy control line UTA.04602.WT was generated using pMX retroviral vectors without Cre-LoxP site, as described earlier [19, 20]. To generate hiPSC lines from the symptomatic (UTA.14,004.*SCN5A*) and asymptomatic (UTA.13,901.*SCN5A*) individuals, fibroblasts were transfected with the 4D-Nucleofector™ System (Lonza, Basel, Switzerland) according to

the manufacturer's protocols and using a plasmid DNA cocktail, as described previously [21]. Plasmid vectors are available from Addgene repository upon request: 27,077 (pCXLE-hOCT3/4-shp53-F), 27,078 (pCXLE-hSK), 27,080 (pCXLE-hUL), and 37,624 (pCXWB-EBNA1). After derivation, hiPSC lines were cultured on mouse embryonic fibroblast feeder cell layers (Merk Millipore, Darmstadt, Germany) as described previously [20]. One line from each subject was used.

The karyotypes, pluripotency, and embryoid body (EB) formation of all hiPSC lines were characterized. The characteristics of the WT hiPSC lines have been reported previously [19, 20]. Endogenous and exogenous gene expressions were examined *via* reverse transcription-polymerase chain reaction (RT-PCR). Detailed reaction conditions and PCR primers for the hiPSC characterization have been published previously [19]. The protein levels of endogenous pluripotency markers were studied *via* immunocytochemistry using antibodies recognizing sex-determining region Y-box 2 (SOX2), the homeobox protein NANOG, tumor-related antigen (TRA)1–81 (all at 1:200, from Santa Cruz Biotechnology, Santa Cruz, CA, USA), and the POU transcription factor OCT3/4 (1:400, R&D Systems) as described previously [22]. Karyotypes of the cell lines were obtained *via* a KaryoLite™ BoBs™ assay (Perkin Elmer) based on the BACs-on-Beads™ technology (Molecular and Systems Immunology and Stem Cell Biology, Turku Centre for Biotechnology, University of Turku, Finland). The expression of markers characteristic from the ectoderm (paired box protein *Pax6*), endoderm (*SOX17*), and mesoderm (vascular endothelial growth factor receptor 2 *VEGF-R2*) development was determined in EBs as described previously [22].

Cardiomyocyte differentiation and characterization

All hiPSC lines were differentiated into spontaneously beating CMs by coculturing them with murine visceral endoderm-like (END-2) cells (from Prof. Mummery, Hubrecht Institute, Utrecht, The Netherlands). Minimum of four differentiation batches were established from each hiPSC lines. For calcium (Ca^{2+}) imaging and patch-clamp studies, minimum of 30 days old beating cell clusters were mechanically excised and treated with collagenase A (Roche Diagnostics, Basel, Switzerland) [23]. Single CMs were then plated on 12- and 5-mm round-glass coverslips coated with 0.1% gelatin. For microelectrode arrays (MEA) (Multichannel systems, Reutlingen, Germany), spontaneously beating cardiac aggregates were dissected and plated on 0.1% gelatin-coated 6-well MEA plates. Single CMs and cardiac aggregates were maintained in EB medium supplemented with 20% fetal bovine serum. For immunofluorescence staining, the CMs were fixed with 4% paraformaldehyde, and the following primary antibodies were used: anti-cardiac troponin T (1:1,500,

Abcam, Cambridge, MA, USA), anti-human $\text{Na}_v1.5$ ($\text{hNa}_v1.5$, 1:200, Alomone Labs, Israel, ASC-005), and anti-SCN7A (1:200, Sigma-Aldrich, HPA004879).

Allelic imbalance and quantitative RT-PCR (qRT-PCR)

To determine the *SCN5A* allelic imbalance in hiPSC-CMs obtained from the asymptomatic and symptomatic subjects, beating CM aggregates were lysed, and total RNAs were purified using Norgen's Total RNA Purification Plus Kit (Norgen Biotek Corp., Ontario, Canada) according to the manufacturer's protocols. RNAs were converted into cDNAs using the High-Capacity cDNA Reverse Transcription Kit (Thermo Fisher Scientific, Massachusetts, USA). Allelic discrimination between WT and mutant *SCN5A* alleles was performed *via* quantitative PCR (qPCR) using standard curves as described before [24, 25]. To generate *SCN5A* allelic standard curves, plasmids containing either WT *SCN5A* or mutant *SCN5A*-p.R1913C allele were generated by amplifying a 576-bp fragment of *SCN5A* containing the mutation site from the cDNA extracted from the UTA.04602.WT cell line. The WT allele fragment was cloned into pBluescript SK+ plasmid (Addgene, Cambridge, MA, USA) using BamHI and NotI restriction enzymes (Thermo Fisher Scientific Inc.). The mutant *SCN5A* plasmid was generated from the WT plasmid using the QuikChange II Site-Directed Mutagenesis Kit (Agilent Technologies Inc., Santa Clara, CA, USA). The primers used for generating the plasmids are listed in additional file 1: Table S1. Both plasmid constructs were sequenced to verify the presence of the correct allele fragment. Plasmids carrying WT and mutant *SCN5A* alleles were combined at the ratios (WT/mutant) of 1/0, 8/1, 4/1, 2/1, 1/1, 1/2, 1/4, 1/8, and 0/1 for the qPCR reactions. For allelic discrimination, the primers and probes were designed by the Custom TaqMan® SNP Genotyping Assay service (Thermo Fisher Scientific). The qPCR analyses were conducted using a 7300 Real-Time PCR System (Applied Biosystems, Life Technologies Ltd.) to determine the C_t values for the different plasmid ratios and the hiPSC-CM cDNA samples. For the plasmid standard curves, the \log_2 values of WT/mutant plasmid ratios were plotted against the corresponding ΔC_t values, which were obtained by subtracting the C_t value measured for the WT *SCN5A* allele from the C_t value measured for the mutant allele. The ΔC_t values for hiPSC-CM samples were measured and plotted on the standard curve to determine the corresponding WT/mutant ratio. In standard curves, the ΔC_t values for plasmid ratios were expressed as means \pm standard deviations (SDs) ($n=3$).

RNA samples were collected and extracted from spontaneously beating WT hiPSC-CMs and hiPSC-CMs derived from the asymptomatic and symptomatic subjects using Norgen's Total RNA Purification Plus Kit

(Norgen Biotek Corp., Ontario, Canada) according to the manufacturer's protocols. The High-Capacity cDNA Reverse Transcription Kit (Applied Biosystems) was used to transcribe 500–1000 ng of RNA into cDNA, and qPCR was performed following standard protocols on the Abi Prism 7300 instrument (Applied Biosystems). Samples were analyzed as triplicates. The expression levels of *cardiac troponin T2 (TNNT2)*, *SCN5A*, *sodium/calcium exchanger 1 precursor (SLC8A1)*, *ryanodine receptor 2 (RYR2)*, *protein phosphatase 3 catalytic subunit alpha (PPP3CA)*, and the endogenous control *glyceraldehyde-3-phosphate dehydrogenase (GAPDH)* were evaluated using TaqMan Universal PCR Master Mix (Applied Biosystems). The following TaqMan assays ($\times 20$) were used: Hs00165960_m1 for *TNNT2*, Hs00165693_m1 for *SCN5A*, Hs01062258_m1 for *SLC8A1*, Hs00892883_m1 for *RYR2*, Hs00174223_m1 for *PPP3CA*, and Hs00270914_m1 for *GAPDH* (Applied Biosystems). The relative expression levels were determined using the comparative method ($\Delta\Delta Ct$) [26]. The gene expressions were normalized to that of *TNNT2*.

Action potential (AP) measurement and video recording

APs were recorded from spontaneously beating hiPSC-CMs in perforated patch configuration using amphotericin B at $36 \pm 1^\circ\text{C}$. Current-clamp recordings were digitally sampled at 20 kHz and filtered at 2 kHz using a low-pass Bessel filter on the recording amplifier. An Axon Series 200B patch-clamp amplifier connected to a Digi-data 1440a AD/DA converter driven by the pCLAMP 11 software (Molecular Devices, California, USA) were used. The patch electrodes had tip resistance of 2.0–3.0 M Ω and contained the following intracellular solution: 132 mM KMeSO₄, 4 mM ethylene glycol-bis (β -aminoethyl ether)-N,N,N',N'-tetraacetic acid (EGTA), 20 mM KCl, 1 mM MgCl₂, and 1 mM CaCl₂ (pH was adjusted to 7.2 with KOH). The extracellular solution contained 143 mM NaCl, 4.8 mM KCl, 1.8 mM CaCl₂, 1.2 mM MgCl₂, 5 mM D-glucose, and 10 mM 4-(2-hydroxyethyl)-1-piperazineethanesulfonic acid (HEPES) (pH was adjusted to 7.4 with KOH). The AP durations at 90%/50% repolarization (APD₉₀/APD₅₀) ratio describe the shape of the repolarization curve and this ratio was used to classify the specific subtype of hiPSC-CMs. Only ventricular-like hiPSC-CMs, characterized by a ratio between AP durations at 90% and at 50% repolarization (APD₉₀/APD₅₀) < 1.35 (indicative of pronounced plateau phase) and an AP amplitude (APA) > 90 mV, were used for comparison. All the drugs and chemicals were purchased from Sigma-Aldrich (Sigma-Aldrich, Saint Louis, USA) unless otherwise specified. KMeSO₄ was ordered from MP Biomedicals (California, USA).

Videos were simultaneously recorded to AP measurements using an ANDOR iXon 885 EM-CCD camera

(Andor Technology, Belfast, Northern Ireland), TH4-200 light source (Olympus, Tokyo, Japan), inverted Olympus IX70 microscope with PhC 0.40NA 20 \times air objective (Olympus), and Live Acquisition software (TILL Photonics, Munich, Germany). Videos were recorded for at least 10 s at 60 frames per second. The pCLAMP software was configured to synchronize data between the patch-clamp and video recordings using synchronization pulses to determine the start and end of the video in the AP recording (additional file 1: Fig S2). From the recorded videos, half-width contraction and relaxation duration were calculated using a custom-made software based on MATLAB (The MathWorks, Massachusetts, USA) [27].

Ionic current measurements

I_{Na} were recorded using whole-cell patch configuration at room temperature. For voltage-clamp experiments, patch pipettes were filled with a solution containing 140 mM cesium methane sulfonate, 5 mM NaCl, 5 mM EGTA, and 10 mM HEPES (pH adjusted to 7.2 with CsOH). The bath solution was composed of 50 mM NaCl, 115 mM tetramethylammonium chloride, 2 mM CaCl₂, 1.2 mM MgCl₂, 5 mM D-glucose, and 10 mM HEPES (pH adjusted to 7.4 with tetramethylammonium hydroxide). To block the Ca²⁺ current, 10- μM nimodipine was added to the extracellular solution. I_{Na} were elicited using step potentials ranging from -60 to 80 mV with 5-mV increments and a holding potential of -100 mV. The membrane capacitance was measured for each cell by integrating the area under the capacitive transient induced by a 5-mV hyperpolarizing step pulse, from -80 to -85 mV, and dividing it by the voltage step. Current densities were calculated by dividing the currents by the capacitance and were expressed as pA/pF. The liquid junction potential was not corrected. Series resistance and cell capacitance were compensated for 40–50%.

The Na⁺ conductance (g_{Na}) was calculated using the equation $g_{\text{Na}} = I_{\text{Na}} / (V_m - E_{\text{Na}})$, where V_m denotes the membrane potential and E_{Na} the Na⁺ reversal potential. The reversal potentials were experimentally determined for each cell. Steady-state voltage dependence of the inactivation was calculated using the double-pulse protocol with a holding potential of -120 mV. The varying 200-ms-long conditioning pulse from -120 to -20 mV ($\Delta V = 5$ mV) protocol was used. The peak I_{Na} were normalized to a maximum value.

Both steady-state activation and inactivation curves were fitted using a Boltzmann equation: $y = A / \{1.0 + \exp[(V_{1/2} - V)/k]\}$, where $V_{1/2}$ denotes the half-maximum (in)activation potential and k the slope factor. Time constants of I_{Na} inactivation were determined by fitting a biexponential equation, $y = A_f \times [1 - \exp(-t/\tau_f)] + A_s \times [1 - \exp(-t/\tau_s)]$, where A_f and A_s are the fractions of the fast and slow inactivation components, respectively, and τ_f

and τ_s are the time constants of the fast and slow inactivation components, respectively.

The time course of the recovery from inactivation was analyzed using the double-pulse protocol. For this, a conditioning pulse (P1) of -20 mV was applied for 50 ms. Then, a test pulse (P2) of -20 mV was applied for 50 ms after different recovery times (5, 10, 20, 50, 100, 200, 300, 400, 500, 600, 700, 800, 900, 1000, or 1500 ms) between each recovery potential. The peak I_{Na} elicited by P2 were normalized (P2/P1) and plotted as a function of the recovery interval. In addition, the time course of entry into the slow inactivation state was analyzed following the double-pulse protocol. For this, P1 at -20 mV was applied for varying durations (5, 10, 20, 50, 100, 200, 300, 400, 500, 600, 700, 800, 900, 1000, 1500, or 2000 ms). They were followed by a step at -120 mV for 50 ms to remove fast inactivation and by P2 at -20 mV for 50 ms to assess channel availability. The peak I_{Na} elicited by P2 were normalized (P2/P1) and plotted as a function of the duration of conditioning pulses.

The rapidly activating delayed rectifier potassium current (I_{Kr}) was recorded in the presence of $5\text{-}\mu\text{M}$ nimodipine in the extracellular solution. I_{Kr} was sensitive to $1\text{-}\mu\text{M}$ E-4031 and elicited from the step potential from -20 to 40 mV with 20-mV increments and a holding potential of -40 mV. The peak and tail currents of I_{Kr} were calculated from the end of the test pulse and the peak of the tail current, respectively.

The Ca^{2+} currents were elicited from the step potential from -50 to 60 mV with 5-mV increments and a holding potential of -40 mV and were sensitive to $5\text{-}\mu\text{M}$ nimodipine. The time course of the recovery from inactivation was analyzed using the double-pulse protocol. For this, P1 of 10 mV was applied for 300 ms. Then, P2 of 10 mV was applied for 300 ms after different recovery times (10, 20, 40, 60, 80, 100, 150, 200, 300, 400, 600, 800, 1000, or 1200 ms) between each recovery potential. The peak I_{Ca} elicited by P2 were normalized (P2/P1) and plotted as a function of the recovery interval. The time course of the entry into the slow inactivation state was also analyzed following the double-pulse protocol. For this, P1 of 10 mV was applied for various durations (20, 40, 60, 80, 100, 200, 300, 400, 600, 800, 1000, 1200, 1500, or 2000 ms). It was followed by a 50-ms step at -40 mV to remove fast inactivation and by P2 at 10 mV for 300 ms to evaluate channel availability. The peak I_{Ca} elicited by P2 were normalized (P2/P1) and plotted as a function of the duration of conditioning pulses.

MEA

MEA recording and analysis were conducted as described previously [28]. For the measurements, CM aggregates were moved into serum-free EB medium 1 h before the experiment. The measurements were performed in the

serum-free EB medium at $36 \text{ }^\circ\text{C} \pm 1 \text{ }^\circ\text{C}$. The beating rate was corrected using Bazzet's equation. Aggregates with a beating rate below 20 or above 90 were not considered to prevent over or under-correction.

Ca^{2+} imaging

Dissociated spontaneously beating CMs were seeded on a coverslip and loaded with $4\text{-}\mu\text{M}$ Fluo-4 AM (Thermo Fisher Scientific). An HEPES-based medium, consisting of 137-mM NaCl, 5-mM KCl, 0.44-mM KH_2PO_4 , 20-mM HEPES, 4.2-mM NaHCO_3 , 5-mM D-glucose, 2-mM CaCl_2 , 1.2-mM MgCl_2 , and 1-Na pyruvate (pH was adjusted to 7.4 with NaOH), was used for Ca^{2+} imaging measurements at $36 \text{ }^\circ\text{C} \pm 1 \text{ }^\circ\text{C}$. The Ca^{2+} kinetics were photographed using an Axio Observer.A1 microscope and an Objective Fluar 20x/0.75 M27 (both Carl Zeiss Microscopy GmbH, Göttingen, Germany). Images were obtained using an ANDOR iXon3 885 EM-CCD camera (Andor Technology, Belfast, Northern Ireland) synchronized with Lambda DG-4 Plus (Sutter Instrument, California, USA) wavelength switcher, ZEISS Filter set 69 (Carl Zeiss Microscopy GmbH, Göttingen, Germany), and ZEN 2 blue edition software (Carl Zeiss Microscopy GmbH, Göttingen, Germany). In addition to baseline measurements, the effects of $1\text{-}\mu\text{M}$ adrenaline (Sigma-Aldrich) and $1\text{-}\mu\text{M}$ flecainide (Sigma-Aldrich), used to induce clinical phenotypes in the hiPSC-CMs, were studied. For the Ca^{2+} analysis, the regions of interest were selected from spontaneously beating cells, and background noise was subtracted before data processing. All recordings lasted at least 30 s, with a sampling rate of 20 to 30 Hz.

Data analysis and statistics

The electrophysiological and MEA data were analyzed using Clampfit version 11.1.0.23 (Molecular Devices) and a custom-made OriginLab program (OriginLab 2018b, Northampton, USA). For the patch-clamp and MEA recordings, comparisons between cell lines were performed with the non-parametric Kruskal–Wallis test followed by Dunn's *post-hoc* multiple comparisons test (GraphPad Prism Version 5.02, San Diego, CA, USA). The Ca^{2+} peak parameters were analyzed using Clampfit (Molecular Devices). In these analyses, the instantaneous frequency was calculated by converting each interevent interval into a frequency and subsequently averaging these frequencies. In addition, Ca^{2+} traces were analyzed by identifying the signals as normal or abnormal and categorizing the abnormalities into subgroups. Data obtained from WT CMs (04511.WT and 04602.WT) were pooled as their Ca^{2+} peak parameter values were similar. Statistical analyses of Ca^{2+} and qRT-PCR data were conducted using the SPSS software version 24 (SPSS, Chicago, IL, USA). Comparisons within cell lines

(before and after drug administration) were performed with non-parametric Wilcoxon and comparisons among cell lines (cell line-to-cell line comparison) with non-parametric Kruskal–Wallis with Bonferroni correction. Statistical significance levels are indicated as “ns” (not significant), * $P < 0.05$, ** $P < 0.01$, or *** $P < 0.001$.

Results

Analysis of hiPSC lines characteristics

We generated hiPSC lines from the skin biopsies of the asymptomatic and symptomatic stepbrothers. The SCN5A-p.R1913C mutation is caused by a single nucleotide change (5737 C>T) and is located in the C-terminus of the SCN5A gene (Fig. 1C). All hiPSC lines were characterized. WT hiPSC line characterization has been published before [19, 20, 29]. The hiPSC lines from the asymptomatic and symptomatic individuals expressed the endogenous pluripotent markers, namely, *NANOG*, *OCT4*, *TRAI-60*, and *TRAI-81* (Fig. 1D). The expression of exogenous reprogramming agents (*OCT3/4*, *Klf4*, *SOX2*, *LIN-28*, and *L-MYC*) was silenced (Fig. 1E), whereas that of endogenous pluripotency genes (*NANOG*, *REX1*, *OCT3/4*, and *SOX2*) was activated (Fig. 1F). Pluripotency of the cell lines was further confirmed by in vitro formation of EBs with all three germ layers (Fig. 1G). The karyotypes of all hiPSC lines were normal.

Biochemical and genetic analyses of hiPSC-derived CMs

Allelic imbalance in CMs derived from both individuals was analyzed by discriminating between WT SCN5A and mutant SCN5A-p.R1913C alleles. The expression ratio between WT and mutant alleles was between 1/1 and 2/1 (WT/mutant) in cell lines obtained from both asymptomatic and symptomatic individuals (Fig. 2A).

Differentiated CMs expressed the cardiac protein marker troponin T and the Na⁺ channel proteins hNa_v1.5 and hNa_v2.1 (Fig. 2B). Immunofluorescence staining revealed no clear differences in the Na⁺ channel protein expressions between WT CMs and CMs from asymptomatic or symptomatic individuals by visual inspection. To confirm and compare the expression of certain ion channel genes, qRT-PCR analyses were conducted. No significant changes in *TNNT2*, *SCN5A*, *SLC8A1*, *RYR2*, and *PPP3CA* gene expression were observed among the three groups (Fig. 2C).

Ionic currents and biophysics

I_{Na} properties were studied in WT CMs (cell line UTA.04602.WT) and in CMs from asymptomatic and symptomatic individuals. Figure 3(A–C) present representative traces of I_{Na} . The mean I_{Na} densities were plotted against the membrane potentials (Fig. 3D). Similar current–voltage relationships were found for all groups,

and the maximum mean I_{Na} densities were observed at -20 mV (Fig. 3D). Although averaged I_{Na} density at -20 mV was approximately 25% greater in CMs from asymptomatic (-26.0 ± 2.9 , $n=21$) and symptomatic (-26.2 ± 3.7 , $n=23$) individuals than that in WT CMs (-20.1 ± 2.6 , $n=30$), there was no significance difference in I_{Na} densities among groups at any tested potentials (Fig. 3D, additional file 1: Table S2). Furthermore, the voltage dependence of I_{Na} activation was assessed from the current–voltage relationship of I_{Na} and plotted against the tested potentials (Fig. 3E). The $V_{1/2}$ and k were calculated by fitting the curves with the Boltzmann distribution from WT CMs ($V_{1/2} = -31.0 \pm 1.1$, $k=6.0 \pm 0.5$; $n=16$) and CMs from asymptomatic ($V_{1/2} = -33.5 \pm 1.0$, $k=5.4 \pm 0.4$; $n=19$) and symptomatic ($V_{1/2} = -31.9 \pm 1.7$, $k=5.1 \pm 0.4$; $n=19$) individuals. No significant difference was observed among the groups (S3A Table). I_{Na} inactivation was also investigated using the voltage protocol presented in Fig. 3F (inset). Similarly, $V_{1/2}$ and k were calculated by fitting the curves with the Boltzmann distribution from WT CMs ($V_{1/2} = -71.5 \pm 2.0$, $k=9.9 \pm 0.4$; $n=19$) and CMs from asymptomatic ($V_{1/2} = -73.1 \pm 1.2$, $k=10.5 \pm 0.3$; $n=19$) and symptomatic ($V_{1/2} = -74.1 \pm 1.5$, $k=10.3 \pm 0.3$; $n=18$) individuals. The values were similar among the groups (additional file 1: Table S3). To analyze the I_{Na} inactivation kinetics, a biexponential function was fitted to I_{Na} elicited at membrane potentials between -30 and 20 mV in WT CMs ($n=20$) and CMs from asymptomatic ($n=17$) and symptomatic ($n=18$) individuals. Then, τ_{fast} and τ_{slow} were calculated and plotted against the membrane potential. Our results indicated that τ_{slow} was similar among the groups, but τ_{fast} obtained with membrane potentials between -15 and 10 mV were significantly smaller in CMs from the asymptomatic and/or symptomatic individuals than that in WT CMs ($P < 0.05$, Fig. 3G) (additional file 1: Table S4).

Additional experiments were conducted to characterize the differences in the time course of the recovery from inactivation using the double-pulse protocol presented in Fig. 3H (inset). These curves were fitted with biexponential equations. Data analysis revealed that τ_{fast} and τ_{slow} were smaller in CMs from asymptomatic (τ_{fast} : 47.4 ± 4.9 and τ_{slow} : 509.2 ± 60.5 ; $n=8$) and symptomatic (τ_{fast} : 63.3 ± 5.7 and τ_{slow} : 579.9 ± 32.3 ; $n=8$) individuals than those in WT CMs (τ_{fast} : 74.8 ± 7.0 and τ_{slow} : 700.3 ± 94.1). However, only the τ_{fast} difference between CMs from the asymptomatic individual and WT CMs was significant ($P < 0.05$) (additional file 1: Table S5A). A smaller τ_{fast} , albeit not significant, was also observed in CMs from the symptomatic stepbrother compared with that of WT CMs (S5A Table). Furthermore, the time course of entry into the slow inactivation state was evaluated using the protocol presented in Fig. 3I (inset). These curves were also fitted with biexponential equations. The comparison

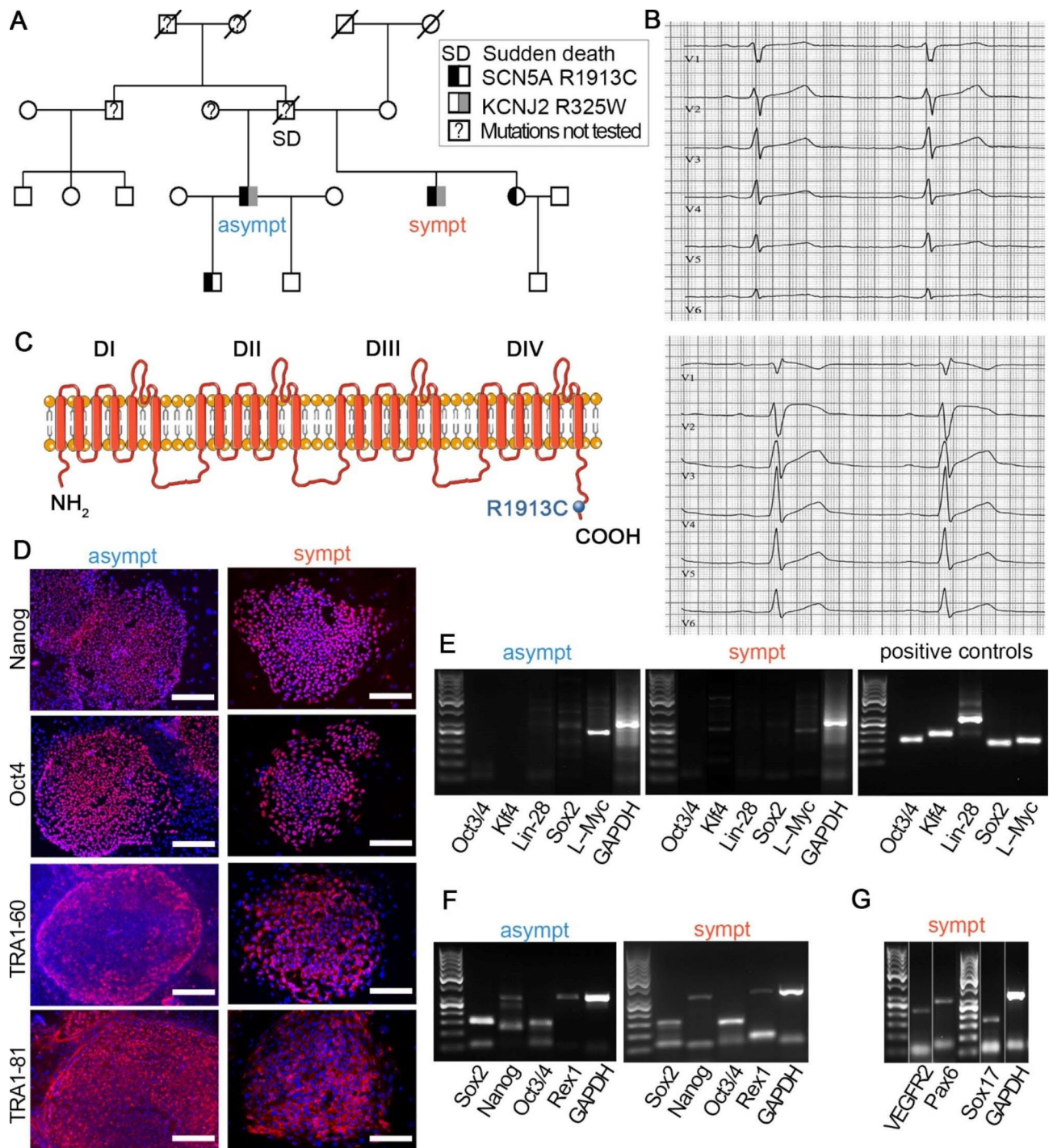


Fig. 1 Clinical background of asymptomatic and symptomatic individuals and generation and characterization of hiPSC-lines. **(A)** The pedigree of the family of asymptomatic (Brugada syndrome) and symptomatic brothers. **(B)** ECG from symptomatic individuals before (above) and 10 min after receiving flecainide (below). **(C)** Schematic representation of *SCN5A* channel protein. Mutation R1913C is located in the C-terminal of the protein. **(D)** Immunocytochemical stainings and expression of pluripotency markers. Scale bars 100 μ m. **(E)** RT-PCR confirmed that none of the exogenous genes are expressed in iPSC lines. Images are cropped and merged, and full images available in additional file 1: Fig S3A **(F)** pluripotency markers are turned on. Images are cropped and merged, and full images available in additional file 1: Fig S3B-C and **(G)** EBs express markers from all the three embryonic germ layers. Images are cropped and merged, and full images available in additional file 1: Fig S3D. GAPDH serves as a housekeeping gene in all RT-PCR figures

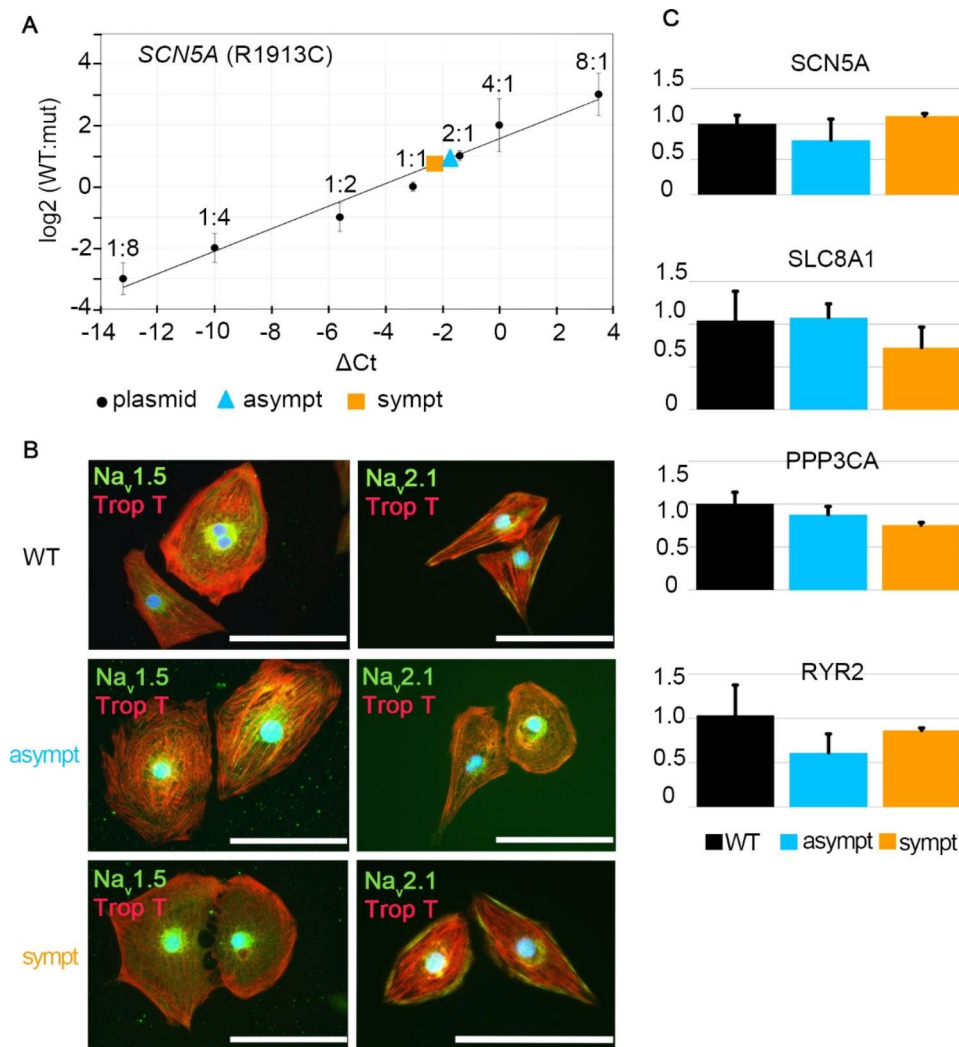


Fig. 2 Characterization of hiPSC-CMs. **(A)** Allelic discriminations between the WT and mutated SCN5A alleles in asymptomatic and symptomatic CMs. **(B)** Immunocytochemical stainings where red represents troponin T, green sodium channel Na_v1.5 and Na_v2.1 and blue DAPI-staining for nuclei. Scale bars 100 μm. **(C)** Relative gene expression levels of cardiac related genes. The GAPDH was used as an endogenous control. No statistically significant differences in expression levels of WT, asymptomatic and symptomatic CMs.

revealed significantly greater τ_{fast} and τ_{slow} in the CMs from the asymptomatic individual than that in WT CMs ($P < 0.05$) (additional file 1: Table S5B).

The I_{Kr} current densities were not significantly different among the groups (additional file 1: Fig. S4A–B). The I_{Ca} current densities were similar between CMs from asymptomatic and symptomatic individuals, with the averaged I_{Ca} current densities being slightly, albeit not significantly, higher than that of WT CMs (additional file 1: Fig. S4C). The time course of recovery after inactivation and of entry into the slow inactivation state of I_{Ca} were also investigated, but neither τ_{fast} nor τ_{slow} were significantly different among the groups (additional file: Fig. S4D–G).

AP characteristics in CMs from asymptomatic and symptomatic individuals

APs were recorded from spontaneously beating WT CMs (cell line UTA.04602.WT) and CMs from asymptomatic and symptomatic individuals. Figure 4 A–C presents representative AP traces. The occurrence of triggered activity (TA) in ventricular-like CMs was quantified and was greater in CMs from asymptomatic (26.8%, $n = 11/41$) and symptomatic (16.7%, $n = 6/36$) individuals than that in WT CMs (3.4%, $n = 1/29$) (Fig. 4D).

The beat per minute (BPM), maximal upstroke velocity (V_{max}), APD_{50} , APD_{90} , APA, and maximum diastolic potential (MDP) of the APs were calculated. BPMs and V_{max} were not significantly different among the groups (Fig. 4E, F). However, APD_{50} and APD_{90} were significantly shorter in CMs from the symptomatic individual

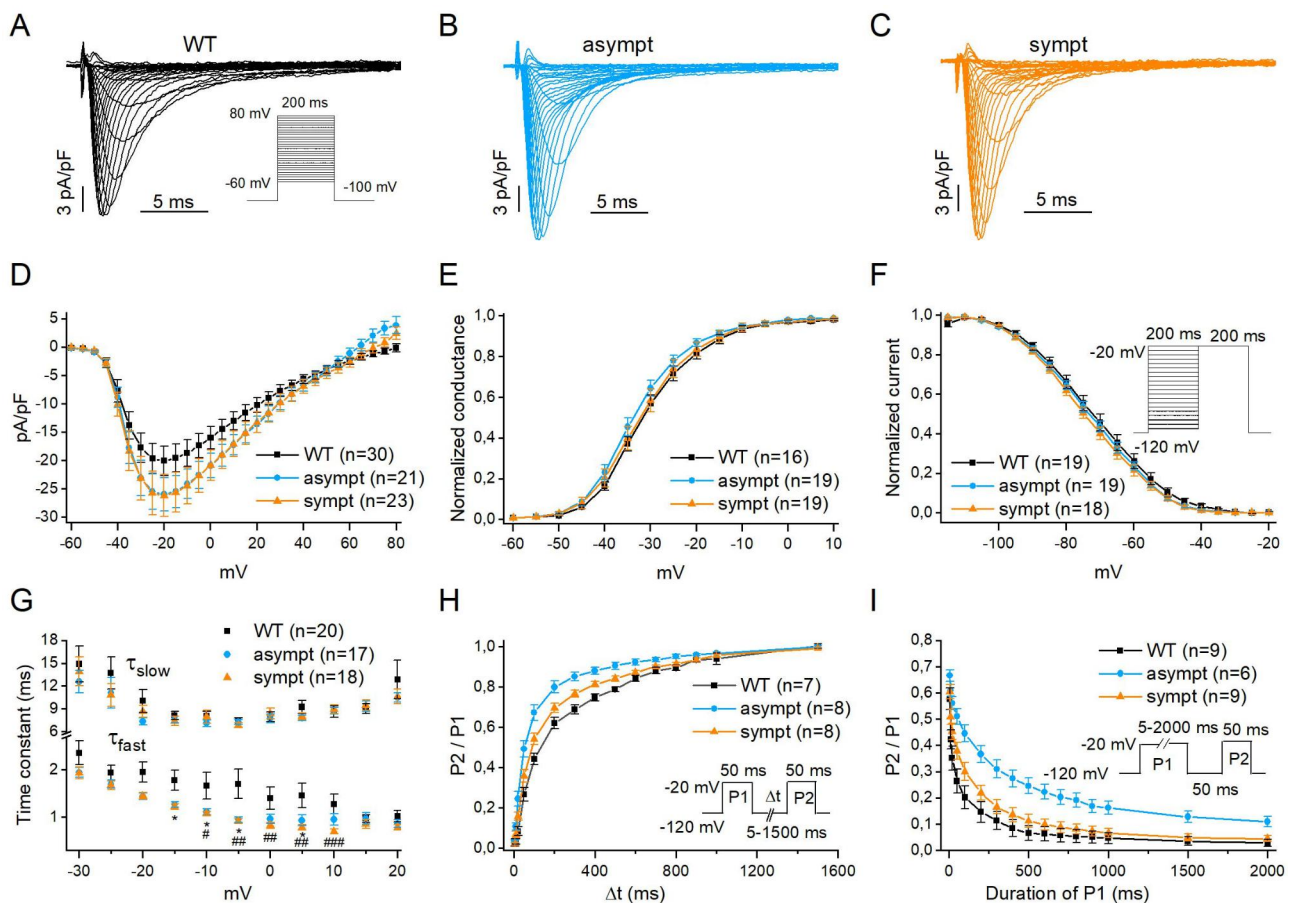


Fig. 3 Sodium current (I_{Na}) densities and gating properties of hiPSC-CMs. (A–C) Typical examples of whole-cell I_{Na} traces recorded at room temperature from WT, asymptomatic and symptomatic CMs. (D) Current–voltage relationships of average I_{Na} densities. (E) Average voltage dependence of activation. (F) Voltage-dependence of steady-state inactivation curve. Peak sodium currents were normalized to maximum values and plotted as function of voltage. (G) Average fast (τ_{fast}) and slow (τ_{slow}) time constants of I_{Na} inactivation plotted as a function of membrane potential. (WT vs. asympt and WT vs. sympt, $*P < 0.05$). (H) Time-course of recovery after inactivation. Peak I_{Na} elicited by P2 were normalized ($P2/P1$) and plotted as function of the recovery interval. (I) The time-course of entry into the slow inactivation state. Peak I_{Na} elicited by P2 were normalized ($P2/P1$) and plotted as function of the duration of P1. Insets: Voltage-clamp protocol used in each experiment. Numbers in parenthesis represent the number of cells used. Data are presented as mean \pm S.E.M.

(APD₅₀: 170.5 ± 11.0 ms, APD₉₀: 207.7 ± 12.4 ms, $n = 36$) compared with those in CMs from the asymptomatic individual (APD₅₀: 224.6 ± 12.1 ms, APD₉₀: 277.5 ± 14.5 ms, $n = 41$) and WT CMs (APD₅₀: 209.9 ± 11.2 ms, APD₉₀: 253.6 ± 13.1 ms, $n = 29$) ($P < 0.05$, Fig. 4G). APA was significantly smaller in CMs from the symptomatic individual (109.5 ± 1.0 mV, $n = 36$) than that in WT CMs (114.8 ± 1.4 , $n = 29$) ($P < 0.05$, Fig. 4H left). The MDP was similar among the groups (Fig. 4H right). Interestingly, a prominent spike-and-dome morphology, which is the cellular equivalent of elevated ST segment observed in ECGs from patients with Brugada syndrome [30] was observed in AP recorded from CMs derived from the symptomatic individual only (Fig. 4I).

Beating characteristics of CMs from asymptomatic and symptomatic individuals

Videos of spontaneously beating WT CMs ($n = 27$) and CMs from asymptomatic ($n = 20$) and symptomatic ($n = 23$) subjects were recorded simultaneously in AP measurements. Figure 5A presents representative traces of normal AP (a) and the corresponding beating traces (b) recorded from WT CMs. TAs were also observed during simultaneous AP acquisition and video recording for CMs from asymptomatic (Fig. 5A c and d) and symptomatic (Fig. 5A e and f) individuals. These arrhythmic behaviors observed in APs (Fig. 5A c and e, marked in arrows) were also detected in the beating of CMs visualized by video recording (Fig. 5A d and f, marked in arrows). Figure 5B presents an image of patch-clamp recording of CMs and a user-selected region of interest for video analysis. Video analysis revealed that contraction and relaxation durations were shorter in CMs from

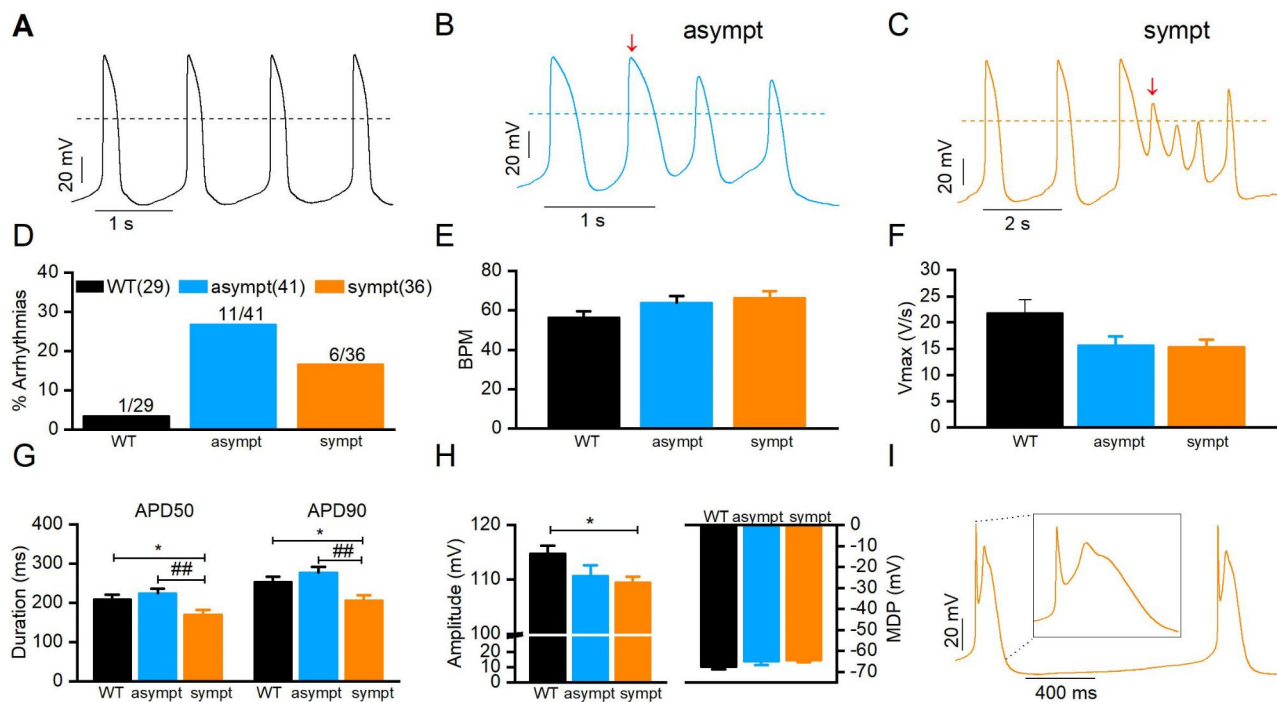


Fig. 4 Action potential (AP) characteristics of ventricular-like CMs. Representative action AP traces from (A) WT, (B) asymptomatic and (C) symptomatic CMs respectively. Arrows indicate the arrhythmias in asymptomatic and symptomatic CMs. (D) Percentage of arrhythmia occurrences in WT (3.4%, $n = 1/29$), asymptomatic ($n = 11/41$) and symptomatic ($n = 6/36$) CMs. Averaged values and comparison of (E) beat per minute (BPM), (F) upstroke velocity (V_{max}), (G) AP duration at 50% (APD50) and 90% (APD90) repolarization, and (H) AP amplitude (APA) and maximum diastolic potential (MDP). (I) Representative AP with prominent spike and dome morphology. Inset: enlarged version of AP. Numbers in parenthesis represent the number of cells used. * or # $P < 0.05$ * WT vs. asympt, # WT vs. sympt. Data are presented as mean \pm S.E.M.

asymptomatic (contraction: 82.3 ± 6.9 ms and relaxation: 97.6 ± 5.5 ms) and symptomatic (contraction: 78.3 ± 4.8 ms and relaxation: 93.8 ± 5.4 ms) individuals than those in WT CMs (contraction: 106.1 ± 9.4 ms and relaxation: 118.3 ± 9.2 ms), but the differences were not statistically significant (Fig. 5C–D and additional file 1: Table S6).

Abnormal MEA measurements in CMs from asymptomatic and symptomatic individuals

The electrophysiological properties of CM aggregates were also evaluated using MEA. Figure 6 A presents representative traces of MEA recording from WT CMs and CMs from the asymptomatic and symptomatic individuals. All CMs had similar beating rates and field potential durations (FPDs) (Fig. 6B, C and S6 Table). The FPDs were corrected with the corresponding beat rates using Bazzet's equation. No significant differences in corrected FPDs were observed among groups (WT: 743.6 ± 21.7 ms, $n = 13$, asymptomatic: 659.4 ± 32.1 ms, $n = 6$, and symptomatic: 755.2 ± 42.5 ms, $n = 19$) (Fig. 6D and additional file 1: Table S7). Moreover, the percentage of arrhythmia in the MEA recording was higher for CMs from asymptomatic (16.7%, $n = 6$) and symptomatic (26.3%, $n = 19$) individuals than that from WT CMs (7.7%, $n = 13$) (Fig. 6E).

Ca²⁺ abnormalities in CMs from asymptomatic and symptomatic individuals

Abnormalities of the Ca²⁺ transients such as oscillations (OS), low amplitude peaks (LP), varying amplitude (VA), plateau abnormality (PA), and delay in the Ca²⁺ upstroke (rise delay, RD) (Fig. 7A) were observed in hiPSC-CMs. Abnormalities were defined as follows: (1) OS were detected if Ca²⁺ oscillated for two or more peaks without reaching the baseline, (2) LP were small amplitude Ca²⁺ events of at least 10% of the preceding Ca²⁺ spike amplitude, (3) PA was detected if the decay time of the Ca²⁺ upstroke was prolonged, (4) RD was detected if the rise time of the Ca²⁺ upstroke was prolonged, and (5) VA was detected if the amplitude of the peaks varied continuously. Transients were considered normal if the trace excluded any of these abnormalities.

More abnormalities of the baseline Ca²⁺ transients were observed in CMs derived from asymptomatic and symptomatic individuals than in WT CMs (51%, 44%, and 18% of the cells, respectively), but there was not much difference between the symptomatic and asymptomatic groups (Fig. 7B). The effects of adrenaline and flecainide were tested to induce the clinical phenotype of Brugada syndrome in CMs. Adrenaline did not impact the percentage of abnormalities in WT CMs or CMs

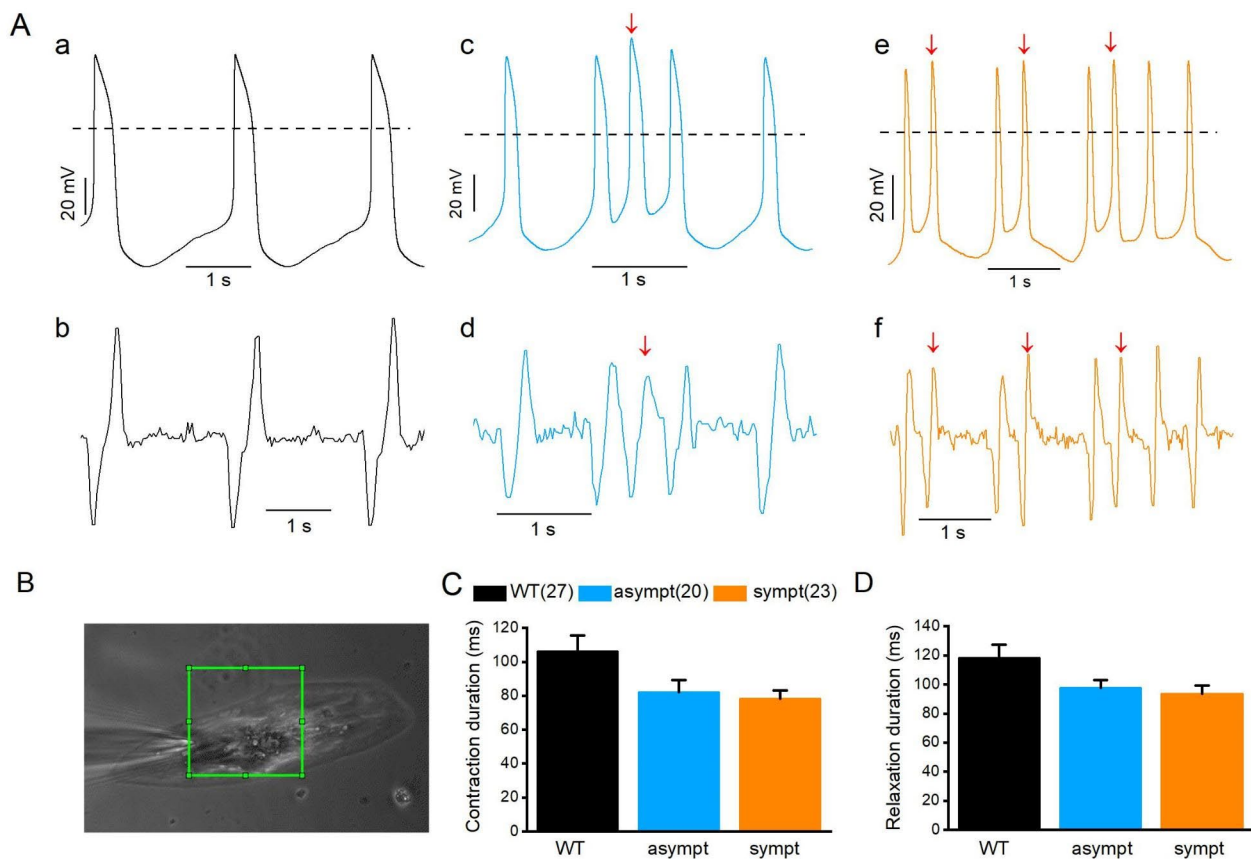


Fig. 5 Simultaneous recording of action potential (AP) and contraction of same cells. **(A)** AP (upper panel) and corresponding beating traces (lower panel) recorded from same cells from WT (a,b), asymptomatic (c,d), and symptomatic (e,f) CMs. **(B)** Image of patch-clamp recording of CM where green rectangle represents the user-selected contraction region of interest. **(C-D)** Comparison of half-width contraction and relaxation durations measured from WT, asymptomatic, and symptomatic CMs. Numbers in parenthesis represent the number of cells used. Data are presented as mean \pm S.E.M.

from the asymptomatic or symptomatic individuals (22%, 46%, and 48% of the cells, respectively) compared with those measured without treatment (Fig. 7B). Flecainide increased the proportion of abnormalities in WT CMs (35%), but not in CMs from asymptomatic and symptomatic individuals (48% and 50% of the cells, respectively, Fig. 7B). In transients of untreated CMs from asymptomatic and symptomatic individuals, the percentages of the different abnormality types were similar, and mostly OS and LP were found. The main effect of adrenaline was the increase in the amount of VA in CMs from the symptomatic individual from 11 to 34% and from the asymptomatic subject from 11 to 20% (Fig. 7C). Flecainide induced an increase in the proportion of PA from 9 to 32% in CMs from the symptomatic individual and VA from 11 to 22% in CMs from the asymptomatic subject (Fig. 7C).

In the absence of treatment, averaged Ca^{2+} peak parameters (additional file 1: Table S8) were significantly different between WT and mutant CMs with lower Ca^{2+} transient amplitudes (F/F₀), Ca^{2+} peak durations (Ca^{90}), half-widths, 90–10% decay times, and interevent

intervals and higher event frequencies in CM from asymptomatic and symptomatic individuals. In addition, the event frequency was significantly higher in CMs from the asymptomatic individual than that in CMs from the symptomatic subject (additional file 1: Table S8). The variation (SD) of Ca^{90} and 10–90% rise time were significantly higher in CMs from asymptomatic and symptomatic subjects than those in WT CMs (Fig. 7D), indicating an abnormal beating pattern of mutated cells. Significantly more variations of the instantaneous frequency were observed in CMs from the asymptomatic individual than in WT CMs and CMs from the symptomatic subject (Fig. 7D).

Adrenaline affected all CMs in a similar way by significantly decreasing F/F₀, Ca^{90} , half-width, 90–10% decay time, and interevent interval and by increasing the event frequency (additional file 1: Table S8). Cytosolic Ca^{2+} transient amplitudes during adrenaline perfusion were significantly lower in CMs from the symptomatic individual than in WT CMs (additional file 1: Table S8). In addition, both types of mutant CMs had significantly

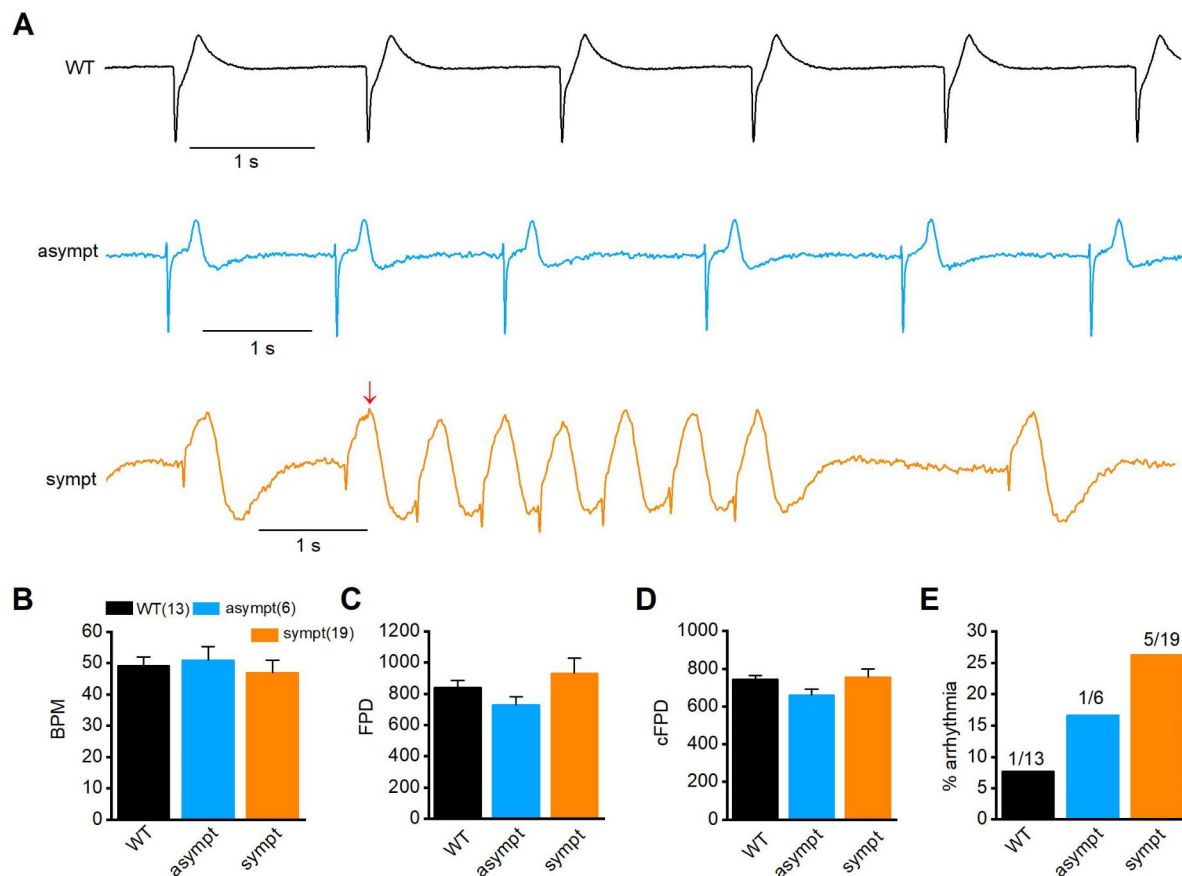


Fig. 6 Characterization of hiPSC-CMs from MEA recording. **(A)** Representative Microelectrode array (MEA) recording from WT (a), asymptomatic (b) and symptomatic-CMs (c). Arrow indicates the initiation of triggered arrhythmia in symptomatic CMs. Comparison of beats per minute **(B)**, field potential duration (FPD) **(C)** corrected FPD **(D)** and **(E)** occurrence of arrhythmias from WT, asymptomatic and symptomatic CMs. Numbers in parenthesis represent the number of cells used. Data are presented as mean \pm S.E.M.

lower Ca^{90} , half-width, 90–10% decay time, and interevent interval and higher event frequency during adrenaline perfusion than those in WT CMs (additional file 1: Table S8). In addition, the interevent intervals were significantly smaller and the event frequency significantly higher in CMs from the asymptomatic subject than those in CMs from the symptomatic individual.

Flecainide affected all CMs in a similar fashion by significantly decreasing cytosolic Ca^{2+} transient amplitudes and event frequencies and by increasing Ca^{90} , half-width, and interevent interval (additional file 1: Table S9). No significant differences were observed in the Ca^{2+} peak parameters among CMs in the absence or presence of flecainide.

Discussion

In this study, we successfully generated hiPSC-CMs from two individuals carrying an SCN5A-p.R1913C mutation. Only one of them showed clinical signs of Brugada syndrome including typical ECG findings, whereas the other

one was clinically asymptomatic, and no ECG changes could be provoked.

The mutant and WT alleles were equally expressed in CMs from asymptomatic and symptomatic individuals and did not account for the different clinical phenotypes of the individuals. A balanced allele expression was also been reported in a previous study on Brugada syndrome using hiPSC-CMs with the SCN5A mutation p.S1812X [14]. In the present work, the Na^+ channel protein and gene expression levels were not significantly different among the symptomatic and asymptomatic SCN5A-p.R1913C mutation carrier CMs and WT CMs. From the voltage-clamp experiments, the I_{Na} were similar in mutant CMs, with a tendency to be higher than that of WT CMs. Similarly, in a Finnish family with an SCN5A-p.I141V mutation, I_{Na} was higher, albeit not significantly, in mutant CMs [31]. Other studies reported a decrease in I_{Na} in hiPSC-CMs obtained from patients with Brugada syndrome and demonstrated a reduced V_{max} in CMs derived from patients compared with that in CMs obtained from healthy subjects [9, 12–15].

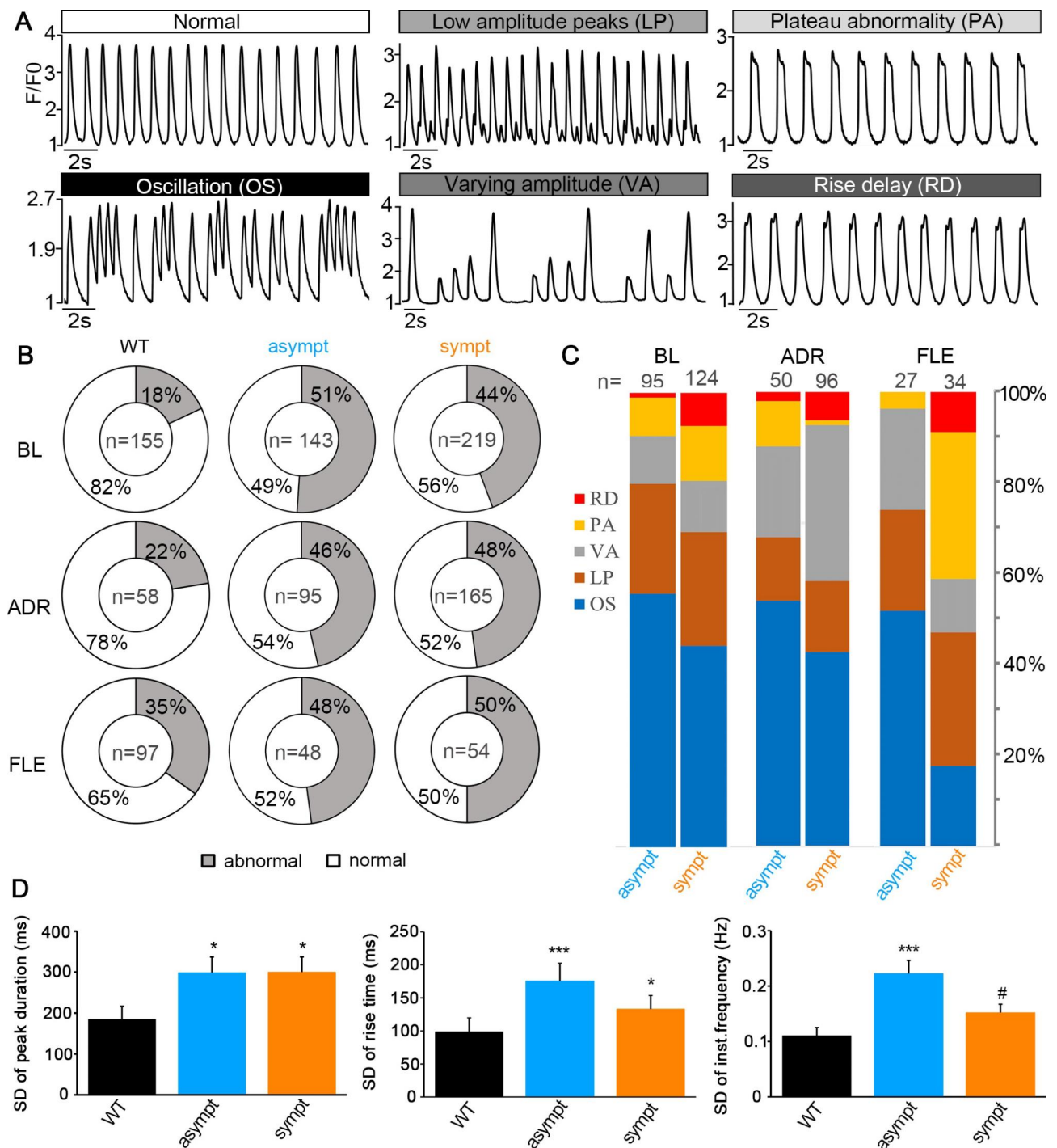


Fig. 7 Ca^{2+} handling abnormalities in hiPSC-CMs. **(A)** Representative traces of a control CM showing normal regular Ca^{2+} transients and mutated CMs showing different abnormality types including oscillations (OS), low amplitude peaks (LP), varying amplitude (VA), plateau abnormality (PA) and rise delay (RD). **(B)** Doughnut charts indicating the abnormality percentage of WT, asymptomatic and symptomatic CMs in baseline and during adrenaline and flecainide perfusion. **(C)** Bar charts indicating the percentage of each abnormality type of asymptomatic and symptomatic CMs in baseline, and during adrenaline and flecainide perfusion. **(D)** Bar graph comparisons of standard deviation (SD) of peak duration, rise time 10–90% and instantaneous frequency of WT (n = 155), asymptomatic (n = 143) and symptomatic (n = 219) CMs in baseline. Data are presented as mean \pm S.E.M. * or # indicates $P < 0.05$ and *** $P < 0.001$. * indicates comparisons with WT CMs and # indicates comparisons with asymptomatic CMs.

Although V_{max} is often used as an I_{Na} indicator [32], a nonlinear relationship between V_{max} and I_{Na} has also been reported [33, 34]. Furthermore, a lower V_{max} in hiPSC-CMs does not always ensure a lower I_{Na} , as CMs might have more positive MDP at which a fraction of Na^+ channels gets inactivated and is thus not functionally available [35]. Our results showed that the SCN5A-p.R1913C mutation results into speeding up the onset of inactivation particular at the voltages where activation of sodium channel reach to the maximum level. Early studies also showed that mutation in sodium channel causing Brugada syndrome result into faster inactivation of the sodium channel [36, 37]. The SCN5A-p.R1913C mutation caused faster inactivation in both symptomatic and asymptomatic hiPSC-CMs. Therefore, the Brugada phenotype cannot be explained solely by inactivation defect. Here, the SCN5A-p.R1913C mutation caused a faster recovery from the inactivation of Na^+ channels. Faster recovery from the inactivation has been shown to result in increased I_{Na} [6]. Furthermore, another study on Brugada syndrome using hiPSC-CMs harboring the SCN5A-p.R367H mutation revealed a faster recovery from inactivation in mutant CMs [11], which is one of the underlying causes of arrhythmia occurrence in patients with Brugada syndrome [38]. In the present work, a higher degree of arrhythmias was observed in AP, intracellular Ca^{2+} , and MEA recordings in CMs from asymptomatic and symptomatic individuals compared with that of WT CMs. There are various mechanisms for the occurrence of the triggered arrhythmias. Earlier study suggest that phase 3 early after depolarization can occur in shorter AP duration as the result of activation of sodium calcium exchanger by larger intracellular calcium at the end of AP [39]. The AP arrhythmias were also reflected in the beating behavior observed on video, thus showing the dependency between the electrical and mechanical activities of CMs. Reduced Ca^{2+} transient amplitudes might lead to insufficient Ca^{2+} release from the sarcoplasmic reticulum and cause an alteration in the Ca^{2+} removal *via* the sarcoplasmic reticulum Ca^{2+} -ATPase and Na^+/Ca^{2+} exchanger [9]. This might lead to the decreased decay time detected in mutant CMs. Some of the Ca^{2+} cycling pathways might be affected in the CMs from patients with Brugada syndrome. The increased arrhythmia might be attributed to increased variations in the beat rate and other parameters, as previously reported [9, 40, 41]. The effects of adrenaline and flecainide were investigated to determine whether the Brugada phenotype could be induced. However, no such phenotypic behavior was observed in Ca^{2+} peak parameters in mutant and WT CMs, although adrenaline induced significant changes in mutant CMs.

The APD in CMs from the symptomatic subject was shorter than that in WT CMs and CMs from the asymptomatic individual. The AP shape and APD depend on

the fine-tuning of inward and outward ionic currents and their interactions [42]. To determine the cause of shorter APD in CMs from the symptomatic subject, we investigated the I_{Kr} and I_{Ca} current densities in WT CMs and mutant CMs. No differences were observed between the mutant lines. In addition, APD also depend on the BPM and hiPSC-CMs from symptomatic individual had the highest BPM, which partially explain the shortest APD. However, the mechanism behind the difference in APD was not fully explained. Other ionic currents, such as the late sodium current, slowly activating delayed rectifier potassium current, transient outward potassium current, inward rectifier potassium current, and Na^+/Ca^{2+} exchanger, also influence the APD [42]. Brugada syndrome is characterized by an ST-segment elevation in the right precordial leads of a 12-lead ECG accompanied by a J wave [30, 43]. The I_{to} -mediated AP notch and loss of the dome mainly in the right ventricle epicardium, but not in the endocardium, cause the transmural voltage gradient during ventricular repolarization and, consequently, the characteristic ECG changes [30]. Here, the spike-and-dome morphology was only observed in the AP of CMs from the symptomatic subject. An early study demonstrated that the spike-and-dome morphology in APs coincides with the J waves in the ECG [43]. Although the mutations occur in all Na^+ channels in the heart, they often manifest only in one chamber, especially the right ventricle. In addition, flecainide inhibits I_{Na} in all CMs, but the Brugada phenotype is particularly observed in the right ventricle [44]. This might be because ionic currents and biophysics of ion channels differ not only between chambers but also between the left and right parts of one chamber [44, 45]. Thus, cardiac diseases should ideally be studied using specific types of CMs. However, it is not possible to obtain region-specific CMs from hiPSCs with high purity, and only a small portion of epicardial-like CMs is yielded using the END-2 differentiation method [46], which hinder the detailed investigation of mechanisms inducing the Brugada phenotype in hiPSC-CMs.

Polygenic risk by common variations in the genetic background and modifiers might cause phenotype differences. Some of these variations might affect cardiac-specific proteins and Na^+ current's biophysical properties, thus inducing different clinical phenotypes among carriers of the same mutation. The link between a mutation and a clinical disease is rarely direct [47]. An individual with Brugada syndrome typically begins exhibiting symptoms around the middle age (average age on diagnostic: 45 years) [48]. Asymptomatic and symptomatic CMs did not fully recapitulate the clinical phenotype of Brugada syndrome possibly due to the inefficient recapitulation of late-onset disease and the lack of maturity of hiPSC-derived cells [49].

The pathophysiology of Brugada syndrome includes various factors beyond the mutation in sodium channels and genetic background and modifiers play an important role [50]. The different genetic backgrounds confer disparate susceptibilities to the effect of mutant sodium channel [7]. Studies showed that only ~50% of the genome is shared between siblings and phenotypic differences could be the result of DNA variants in the other ~50% of the genome rather than the disease-associated mutations [51]. Thus, different genetic background from two different mothers of two patients might have an effect in the results. Another limitation in this study is that the healthy individual is not from the same family. Adding one more control from the same family would have strengthened our results. An ideal control for this study would be the genome edited hiPSC-CMs with same genetic background and difference is only the absence of mutation [51]. However, genome editing of this mutation is left for the further studies. In addition, we had some technical limitation also existed in this study. The frame rate of the video recording was limited and video recording at higher frame rate could be able to record smaller change in membrane potential. Furthermore, we only use one iPSC line from all individuals. Addition of one more clone line from all individuals might strengthen our results. Furthermore, the limitation of immaturity of hiPSC-CMs should also be considered. It might cause different expression profiles of ion channels, lower V_{max} and I_{Na} , which might explain the lack of consistency between the cellular phenotype and the clinical findings in the patient [52]. Although the main strength of hiPSC-CMs is that they carry same genetic background as the donors, our experimental condition does not properly mimic the physiological condition since the experiments were conducted on two-dimensional cell culture [53, 54]. A three-dimensional culture environment could be crucial not only to replicate an *in vivo* microenvironment, but also to improve the maturity of hiPSC-CMs [53, 54].

Finally, differences in gene expression and epigenetic signature might constitute additional phenotype-modifying factors. New information about disease modifiers is needed for the effective diagnosis and treatment of patients.

List of Abbreviations

AP	Action Potential
APA	Action Potential Amplitude
APD ₅₀	Action Potential Duration at 50% repolarization
APD ₉₀	Action Potential duration at 90% repolarization
BPM	Beat Per Minute
Ca ²⁺	Calcium
cFPD	corrected Field Potential Duration
CMs	Cardiomyocytes
V _{max}	Maximal upstroke velocity

EB	Embryoid Body
ECG	Electrocardiogram
FPD	Field Potential Duration
hiPSC	Human Induce Pluripotent Stem Cell
hiPSC-CMs	Human Induced Pluripotent Stem Cell derived Cardiomyocytes
I_{Na}	Sodium Current
MDP	Maximum Diastolic Potential
MEA	Micro Electrode Array
Na ⁺	Sodium
Na _v 1.5	Cardiac Sodium Channel
TA	Triggered Activity
V _{1/2}	Half-maximum (in)activation Potential
k	Slope
τ _f	Time constants of the fast-inactivating component
τ _s	Time constants of the slow-inactivating components

Supplementary Information

The online version contains supplementary material available at <https://doi.org/10.1186/s12872-023-03234-7>.

Additional File: SPIRIT 2013 Checklist: Recommended items to address in a clinical trial protocol and related documents

Acknowledgements

We thank Henna Lappi and Markus Haponen for technical support. The authors acknowledge Tampere Faculty of Electrophysiological Measurements for their service.

Author Contribution

KP and CP contributed equally in this manuscript. KP and CP performed experiments and wrote the main manuscript and prepared figures. DS performed the MEA experiment. RC performed the gene analysis experiment. DR analyzed the video data. HS involved in clinical parts. KAS contributed to study design, supervision, and funding acquisition. All authors reviewed the manuscript.

Funding

Open access funding provided by Tampere University including Tampere University Hospital, Tampere University of Applied Sciences (TUNI).

Data Availability

All data generated or analysed during this study are included in this published article [and its supplementary information files].

Declarations

Ethics approval guidelines and consent to participate

The hiPSC study was approved by the ethical committee of the Pirkanmaa Hospital District (R08070), and written informed consent was obtained from the participants. All methods were carried out in accordance with relevant guidelines and regulations.

Consent for publication

Not applicable.

Competing interests

The authors declare no conflict of interest. The funders had no role in the design of the study; in the collection, analyses, or interpretation of data; in the writing of the manuscript, or in the decision to publish the results.

Received: 14 November 2022 / Accepted: 11 April 2023

Published online: 25 April 2023

References

- Antzelevitch C, Brugada P, Borggrefe M, Brugada J, Brugada R, Corrado D et al. Brugada syndrome: report of the second consensus conference: endorsed by the Heart Rhythm Society and the European Heart Rhythm Association. *Circulation*. 2005;111:659–70.
- Brugada P, Brugada J. Right bundle branch block, persistent ST segment elevation and sudden cardiac death: a distinct clinical and electrocardiographic syndrome. A multicenter report. *J Am Coll Cardiol*. 1992;20:1391–6.
- Brugada P, Brugada R, Brugada J, Geelen P. Use of the prophylactic implantable cardioverter defibrillator for patients with normal hearts. In: *American Journal of Cardiology*. 1999. p.98–100.
- Gourraud JB, Barc J, Thollet A, Le Scouarnec S, Le Marec H, Schott JJ et al. The Brugada Syndrome: A Rare Arrhythmia Disorder with Complex Inheritance. *Frontiers in Cardiovascular Medicine*. 2016;9.
- Chen Q, Kirsch GE, Zhang D, Brugada R, Brugada J, Brugada P, et al. Genetic basis and molecular mechanism for idiopathic ventricular fibrillation. *Nature*. 1998;392:293–6.
- Ortiz-Bonnin B, Rinné S, Moss R, Streit AK, Scharf M, Richter K, et al. Electrophysiological characterization of a large set of novel variants in the SCN5A-gene: identification of novel LQTS3 and BrS mutations. *Pflügers Arch - Eur J Physiol*. 2016;468:1375–87.
- Probst V, Wilde AAM, Barc J, Sacher F, Babuty D, Mabo P, et al. SCN5A mutations and the role of genetic background in the pathophysiology of Brugada syndrome. *Circ Cardiovasc Genet*. 2009;2:552–7.
- Liang P, Lan F, Lee AS, Gong T, Sanchez-Freire V, Wang Y, et al. Drug screening using a library of human induced pluripotent stem cell-derived cardiomyocytes reveals disease-specific patterns of cardiotoxicity. *Circulation*. 2013;127:1677–91.
- Liang P, Sallam K, Wu H, Li Y, Itzhaki I, Garg P, et al. Patient-specific and genome-edited Induced Pluripotent Stem cell-derived cardiomyocytes elucidate single-cell phenotype of Brugada Syndrome. *J Am Coll Cardiol*. 2016;68:2086–96.
- Kosmidis G, Veerman CC, Casini S, Verkerk AO, Van De Pas S, Bellin M et al. Readthrough-promoting drugs gentamicin and PTC124 Fail to Rescue Na v 1.5 function of human-induced pluripotent stem cell-derived cardiomyocytes carrying nonsense mutations in the sodium channel gene SCN5A. *Circ Arrhythmia Electrophysiol*. 2016;9.
- Selga E, Sendfeld F, Martinez-Moreno R, Medine CN, Tura-Ceide O, Wilmut SI, et al. Sodium channel current loss of function in induced pluripotent stem cell-derived cardiomyocytes from a Brugada syndrome patient. *J Mol Cell Cardiol*. 2018;114:10–9.
- Ma D, Liu Z, Loh LJ, Zhao Y, Li G, Liew R, et al. Identification of an INa-dependent and Ito-mediated proarrhythmic mechanism in cardiomyocytes derived from pluripotent stem cells of a Brugada syndrome patient. *Sci Rep*. 2018;8:11246.
- de la Roche J, Angsutararux P, Kempf H, Janan M, Bolesani E, Thiemann S, et al. Comparing human iPSC-cardiomyocytes versus HEK293T cells unveils disease-causing effects of Brugada mutation A735V of NaV1.5 sodium channels. *Sci Rep*. 2019;9:11173.
- Li W, Stauske M, Luo X, Wagner S, Vollrath M, Mehnert CS, et al. Disease Phenotypes and Mechanisms of iPSC-Derived Cardiomyocytes from Brugada Syndrome patients with a loss-of-function SCN5A mutation. *Front Cell Dev Biol*. 2020;8:592893.
- Veerman CC, Mengarelli I, Guan K, Stauske M, Barc J, Tan HL et al. HiPSC-derived cardiomyocytes from Brugada Syndrome patients without identified mutations do not exhibit clear cellular electrophysiological abnormalities. *Sci Rep*. 2016;6.
- Zhong R, Schimanski T, Zhang F, Lan H, Hohn A, Xu Q et al. A Preclinical Study on Brugada Syndrome with a CACNB2 Variant Using Human Cardiomyocytes from Induced Pluripotent Stem Cells. *International Journal of Molecular Sciences*. 2022;23.
- Okata S, Yuasa S, Suzuki T, Ito S, Makita N, Yoshida T, et al. Embryonic type na + channel β -subunit, SCN3B masks the disease phenotype of Brugada syndrome. *Sci Rep*. 2016;6:34198.
- Takahashi K, Tanabe K, Ohnuki M, Narita M, Ichisaka T, Tomoda K, et al. Induction of pluripotent stem cells from adult human fibroblasts by defined factors. *Cell*. 2007. <https://doi.org/10.1016/j.cell.2007.11.019>
- Lahti AL, Kujala VJ, Chapman H, Koivisto AP, Pekkanen-Mattila M, Kerkelä E, et al. Model for long QT syndrome type 2 using human iPSC cells demonstrates arrhythmogenic characteristics in cell culture. *DMM Dis Model Mech*. 2012. <https://doi.org/10.1242/dmm.008409>
- Ojala M, Prajapati C, Pölönen RPR-P, Rajala K, Pekkanen-Mattila M, Rasku J et al. Mutation-specific phenotypes in hiPSC-derived cardiomyocytes carrying either myosin-binding protein C or α -tropomyosin mutation for hypertrophic cardiomyopathy. *Stem Cells Int*. 2016;2016.
- Manzini S, Viiri LE, Marttila S, Aalto-Setälä K. A comparative view on Easy to deploy non-integrating methods for patient-specific iPSC production. *Stem Cell Rev Reports*. 2015;11:900–8.
- Penttinen K, Swan H, Vanninen S, Paavola J, Lahtinen AM, Kontula K et al. Antiarrhythmic effects of dantrolene in patients with catecholaminergic polymorphic ventricular tachycardia and replication of the responses using iPSC models. *PLoS One*. 2015;10.
- Mummery C, Ward-van Oostwaard D, Doevendans P, Spijkier R, Van den Brink S, Hassink R, et al. Differentiation of human embryonic stem cells to cardiomyocytes: role of coculture with visceral endoderm-like cells. *Circulation*. 2003. <https://doi.org/10.1161/01.CIR.0000068356.38592.68>
- Moretti A, Bellin M, Welling A, Jung CB, Lam JT, Bott-Flügel L, et al. Patient-specific Induced Pluripotent stem-cell models for Long-QT syndrome. *N Engl J Med*. 2010;363:1397–409.
- Kiviahho AL, Ahola A, Larsson K, Penttinen K, Swan H, Pekkanen-Mattila M, et al. Distinct electrophysiological and mechanical beating phenotypes of long QT syndrome type 1-specific cardiomyocytes carrying different mutations. *IJC Heart Vasc*. 2015;8:19–31.
- Livak KJ, Schmittgen TD. Analysis of relative gene expression data using real-time quantitative PCR and the 2 $^{-\Delta\Delta CT}$ method. *Methods*. 2001;25:402–8.
- Rajan DK, Maki AJ, Pekkanen-Mattila M, Kreutzer J, Ryyanen T, Valimäki H, et al. Cardiomyocytes: analysis of temperature response and signal propagation between dissociated clusters using Novel Video-Based Movement Analysis Software. *IEEE Access*. 2020;8:109275–88.
- Shah D, Virtanen L, Prajapati C, Kiamehr M, Gullmets J, West G, et al. Modeling of LMNA-Related dilated Cardiomyopathy using Human Induced Pluripotent Stem cells. *Cells*. 2019;8:594.
- Kujala K, Paavola J, Lahti A, Larsson K, Pekkanen-Mattila M, Viitasalo M et al. Cell Model of Catecholaminergic Polymorphic Ventricular Tachycardia Reveals Early and Delayed Afterdepolarizations. *PLoS One*. 2012;7.
- Yan GX, Antzelevitch C. Cellular basis for the Brugada syndrome and other mechanisms of arrhythmogenesis associated with ST-segment elevation. *Circulation*. 1999;100:1660–6.
- Swan H, Amarouch MY, Leinonen J, Marjamaa A, Kucera JP, Laitinen-Forsblom PJ, et al. Gain-of-function mutation of the SCN5A gene causes exercise-induced polymorphic ventricular arrhythmias. *Circ Cardiovasc Genet*. 2014;7:771–81.
- Berecki G, Wilders R, de Jonge B, van Ginneken ACG, Verkerk AO. Re-evaluation of the action potential upstroke velocity as a measure of the na + current in cardiac myocytes at physiological conditions. *PLoS ONE*. 2010;5:e15772–2.
- Sheets MF, Hanck DA, Fozzard HA. Nonlinear relation between V(max) and I(na) in canine cardiac purkinje cells. *Circ Res*. 1988;63:386–98.
- Cohen CJ, Bean BP, Tsien RW. Maximal upstroke velocity as an index of available sodium conductance. Comparison of maximal upstroke velocity and voltage clamp measurements of sodium current in rabbit Purkinje fibers. *Circ Res*. 1984;54:636–51.
- Casini S, Verkerk AO, Remme CA. Human iPSC-Derived cardiomyocytes for investigation of Disease Mechanisms and therapeutic strategies in inherited Arrhythmia Syndromes: Strengths and Limitations. *Cardiovasc drugs Ther*. 2017;31:325–44.
- Rivolta I, Abriel H, Tateyama M, Liu H, Memmi M, Vardas P, et al. Inherited Brugada and Long QT-3 syndrome mutations of a single Residue of the Cardiac Sodium Channel Confer distinct Channel and clinical Phenotypes*. *J Biol Chem*. 2001;276:30623–30.
- Shirai N, Makita N, Sasaki K, Yokoi H, Sakuma I, Sakurada H, et al. A mutant cardiac sodium channel with multiple biophysical defects associated with overlapping clinical features of Brugada syndrome and cardiac conduction disease. *Cardiovasc Res*. 2002;53:348–54.
- Ihor G, Charles A, Preben B, Jeffrey A T, Bernard R C. The Brugada syndrome: clinical, electrophysiologic and genetic aspects. *J Am Coll Cardiol*. 1999;33:5–15.
- Ogawa M, Morita N, Tang L, Karagueuzian HS, Weiss JN, Lin S-F, et al. Mechanisms of recurrent ventricular fibrillation in a rabbit model of pacing-induced heart failure. *Hear Rhythm*. 2009;6:784–92.
- Shah D, Prajapati C, Penttinen K, Cherian RM, Koivumäki JT, Alexanova A, et al. hiPSC-Derived cardiomyocyte model of LQT2 syndrome derived from asymptomatic and symptomatic mutation carriers reproduces clinical differences

- in aggregates but not in single cells. *Cells*. 2020. <https://doi.org/10.3390/cells9051153>
41. Prajapati C, Ojala M, Aalto-Setälä K. Divergent effects of adrenaline in human induced pluripotent stem cell-derived cardiomyocytes obtained from hypertrophic cardiomyopathy. *Dis Model Mech*. 2018. <https://doi.org/10.1242/dmm.032896>
 42. Varró A, Tomek J, Nagy N, Virág L, Passini E, Rodriguez B, et al. Cardiac transmembrane ion channels and action potentials: cellular physiology and arrhythmogenic behavior. *Physiol Rev*. 2020;101:1083–176.
 43. Yan G-X, Antzelevitch C. Cellular basis for the Electrocardiographic J Wave. *Circulation*. 1996;93:372–9.
 44. Calloe K, Aistrup GL, Di Diego JM, Goodrow RJ, Treat JA, Cordeiro JM. Inter-ventricular differences in sodium current and its potential role in Brugada syndrome. *Physiol Rep*. 2018;6:e13787.
 45. Bartos DC, Grandi E, Ripplinger CM. Ion channels in the heart. *Compr Physiol*. 2015;5:1423–64.
 46. Prajapati C, Ojala M, Lappi H, Aalto-Setälä K, Pekkanen-Mattila M. Electrophysiological evaluation of human induced pluripotent stem cell-derived cardiomyocytes obtained by different methods. *Stem Cell Res*. 2021;51:102176.
 47. Jansweijer JA, van Spaendonck-Zwarts KY, Tanck MWT, van Tintelen JP, Christiaans I, van der Smagt JJ, et al. Heritability in genetic heart disease: the role of genetic background. *Open Hear*. 2019;6:e000929.
 48. Minier M, Probst V, Berthome P, Tixier R, Briand J, Geoffroy O, et al. Age at diagnosis of Brugada syndrome: influence on clinical characteristics and risk of arrhythmia. *Hear Rhythm*. 2020;17:743–9.
 49. Doss MX, Sachinidis A. Current Challenges of iPSC-Based Disease modeling and therapeutic implications. *Cells*. 2019;8:403.
 50. Verkerk AO, Amin AS, Remme CA. Disease Modifiers of Inherited SCN5A Channelopathy. *Frontiers in Cardiovascular Medicine*. 2018;5.
 51. Musunuru K. Genome editing of human pluripotent stem cells to generate human cellular disease models. *Dis Model Mech*. 2013;6:896–904.
 52. Li Y, Lang S, Akin I, Zhou X, El-Battrawy I. Brugada Syndrome: different experimental models and the role of Human Cardiomyocytes from Induced Pluripotent Stem cells. *J Am Heart Assoc*. 2022;11:e024410.
 53. Nijak A, Saenen J, Labro AJ, Schepers D, Loeys BL, Alaerts M. iPSC-Cardiomyocyte Models of Brugada Syndrome—Achievements, Challenges and Future Perspectives. *International Journal of Molecular Sciences*. 2021;22.
 54. Varzideh F, Mone P, Santulli G. Bioengineering Strategies to Create 3D Cardiac Constructs from Human Induced Pluripotent Stem Cells. *Bioengineering*. 2022;9.

Publisher's Note

Springer Nature remains neutral with regard to jurisdictional claims in published maps and institutional affiliations.